



D3.4

Impact of stable defect configurations on performances and scaling of HfO₂-based Fe-devices

Andrea Padovani, Anna Kimmel, Miguel Pruneda, Johanner Ocker, Sergiu Clima,
Ben Kaczer, and Arrigo Calzolari

Deliverable D3.4
Impact of stable defect configurations on performances
and scaling of HfO₂-based Fe-devices

Document information

Project acronym:	INTERSECT
Project full title:	Interoperable Material-to-Device simulation box for disruptive electronics
Research Action Project type:	Accelerating the uptake of materials modelling software (IA)
EC Grant agreement no.:	814487
Project starting / end date:	1 st January 2019 (M1) / 30th April 2022 (M40)
Website:	www.intersect-project.eu
Final version:	29/04/2022
Deliverable No.:	D3.4
Responsible participant:	AMAT (participant number 8)
Contributing Consortium members:	ICN2, FMC, IMEC
Due date of deliverable:	30/04/2022
Actual submission date:	29/04/2022
Dissemination level:	PU - Public

Authors: Andrea Padovani, Anna Kimmel, Miguel Pruneda, Johannes Ocker, Sergiu Clima, Ben Kaczer, and Arrigo Calzolari

To be cited as: A. Padovani, A. Kimmel, M. Prouneda, J. Ocker, S. Clima, B. Kaczer, and A. Calzolari (2022): Impact of stable defect configurations on performances and scaling of HfO₂-based Fe-devices. Deliverable D3.4 of the H2020 project INTERSECT (final version as of 28/04/2022). EC grant agreement no: 814487, AMAT, Reggio Emilia, Italy

Disclaimer:

This document's contents are not intended to replace consultation of any applicable legal sources or the necessary advice of a legal expert, where appropriate. All information in this document is provided "as is" and no guarantee or warranty is given that the information is fit for any particular purpose. The user, therefore, uses the information at its sole risk and



liability. For the avoidance of all doubts, the European Commission has no liability in respect of this document, which is merely representing the authors' view.

Deliverable D3.4
Impact of stable defect configurations on performances
and scaling of HfO₂-based Fe-devices

Versioning and Contribution History

Version	Date	Modified by	Modification reason
v.01	15/04/2022	Andrea Padovani	First version
v.02	21/04/2022	Miguel Pruneda and Johannes Ocker	First Revision
v.03	25/04/2022	Ben Kaczer	Second Revision
v.04	28/04/2022	Arrigo Calzolari	Final version

Content

Executive Summary	6
1. Introduction	6
1.1 About this document	7
2. The Material-to-Device workflow of the IM2D box	7
3. DFT Calculations of Material and Defect Properties of the ferroelectric films	8
3.1 DFT characterization of HfO ₂	8
3.2 Modeling TiN/HfO ₂ nanocapacitor	13
3.2.1 System setup	13
3.2.2 Properties of ideal HfO ₂ /TiN short-circuited nanocapacitor	14
3.2.3 Electrostatic potential	15
3.2.4 Formation of Oxygen vacancies	17
4. DFT-based Ferroelectric Device Simulations	19
4.1 Ginestra® Ferroelectric Model	19
4.2 FE Simulations: Results and Discussion	19
4.2.1 Device simulation approach	20
4.2.2 Charge trapping effect on ferroelectric switching hysteresis and speed	20
4.2.3 Impact of HfO _x traps on domain nucleation and variability	21
4.3 FeFET modelling	23
5 Experimental data	28
References	35
Acronyms ¹	36

¹ Acronyms are marked in purple in the text and defined at the end of the document.

Executive Summary

This document provides a description of the use of the material cycle of the Interoperable Materials to Device (IM2D) Simulation box to investigate the effects of material and defect properties, calculated through Density Functional Theory (DFT), on the performance of Ferroelectric (FE) devices.

The task activities rely on the use of Density Functional Theory (DFT) calculations to determine key material properties (e.g. phase, band-gap, defect transition energy) and identify the relevant atomic defects in ferroelectric films with different dopants (Si, Zr). Furthermore, DFT approach is used to study the properties of the HfO₂/TiN nanocapacitors. We characterized the stability, the interfacial structure, the electrostatic potential and the electronic properties of the capacitor system in its ideal configuration, as well as in the presence of oxygen vacancy defects.

Results obtained from DFT are then used as inputs in FE device simulations, performed Ginestra® code connected to the IM2D box. The Ginestra® *FE module* is used to simulate the electrical characteristics and the reliability of the devices. We evaluate the impact that changes in material properties (especially oxygen vacancies) have on its electrical behavior (e.g., switching hysteresis, switching speed). A set of experimental FE devices realized by IMEC completes this investigation.

1. Introduction

One of the goals behind the INTERSECT project is to setup an Interoperable Materials to Device (IM2D) framework able to integrate materials modelling codes, in a way that permits mutual interaction and exchange of information. To test the IM2D simulation box infrastructure, we identified two pilot cases to be used for piloting and testing (see DoA): one on ferroelectric-based devices one, on chalcogenide-based selectors.

This report focuses on the pilot case for the development of solutions for FE materials. Results for chalcogenide pilot are reported in Deliverable D3.2² and D3.5³. More specifically, the present report addresses the material-to-device (M2D) workflow, that is, the use of DFT methods to compute material properties to be used in device-level simulations to understand (and *predict*) their impact on the device electrical behavior. DFT simulations have been

² <https://intersect-project.eu/wp-content/uploads/2022/04/D3.2.pdf>

³ Available on INTERSECT website <https://intersect-project.eu/project-reports/> after submission.

performed to investigate the main electronic properties of HfO₂ in the bulk phase (several crystalline structures) and in TiN/hafnia interfaces. In both cases, we focused on the stability and on the effect of the main point defects, especially the oxygen vacancies that are known to play (see also Sec. 4) a critical role the electrical response of FE devices. Two sets of FE devices have been investigated, namely Fe capacitors (**FeCap**) and Fe-field effect transistors (**FeFET**). Calculations presented here have been performed using the beta versions of the IM2D code implemented in WP1-2. Finally, we report on the fabrication and the characterization of experimental FeFETs and Fe-Caps, where the effect of composition (e.g. doping) is correlated to the FE polarization effects of the devices.

1.1 About this document

The content of this deliverable is related to Task 3.2 (“FE-transistor and FE-memories: Modelling defect impact”), concerning the application of the IM2D toolbox to pilot case on ferroelectric devices. Along with D3.1⁴ it completes the research activity about the development of material/device solutions for novel ultra-low power ferroelectric HfO₂-based logic and memory devices.

2. The Material-to-Device workflow of the IM2D box

Figure 1 shows a schematic representation of the material-to-device workflow of the IM2D simulation box, whose main purpose is to optimize and guide device design by understanding and predicting its performance starting from DFT-computed material properties.

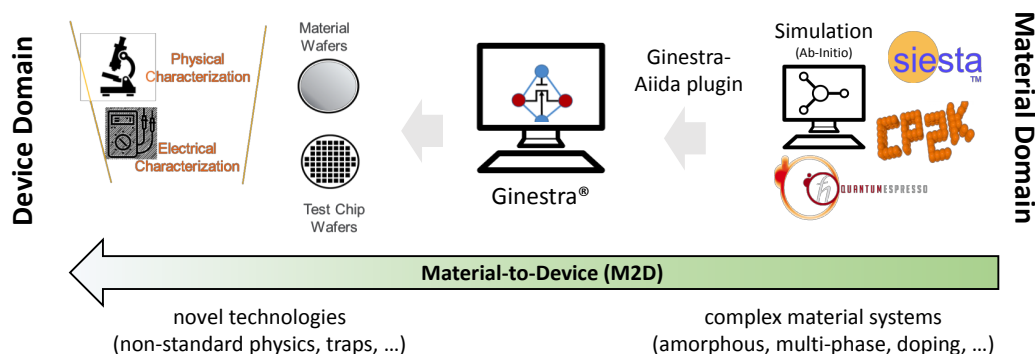


Figure 1. Schematic representation of the M2D workflow.

⁴ <https://intersect-project.eu/wp-content/uploads/2022/04/D3.1.pdf>

The workflow starts from the material domain, where DFT codes are used to compute key properties of the material system of interest (for example bandgap, trap properties, metal-material interface, etc.). The results of DFT calculations represent the input (they can be gathered automatically through the Ginestra-Aiida plugin developed within the project) to subsequent device simulations, whose scope is to evaluate the impact of the computed properties on the device performance and electrical characteristics. The M2D simulation flow enables a virtualization of the device fabrication process that allows one to understand the impact of process and material variations and identify the most promising process and technology solutions before going to the real device fabrication. Semiconductor companies can then fabricate and characterize only the identified solutions, thus reducing costs (for technology development and fabrication) and time-to-market.

3. DFT Calculations of Material and Defect Properties of the ferroelectric films

3.1 DFT characterization of HfO₂

Hafnium dioxide (HfO₂, aka hafnia) is probably the most important high-k insulator in today CMOS technology. Recently, a multitude of the prospective applications of hafnia appeared thanks to discovery of the metastable orthorhombic phase that exhibits ferroelectric behavior. It opened the door for the exploration of ferroelectric capacitor for FERAM, FeFET, non-volatile-memory etc.

Reliability of hafnia-based devices has always been a concern: the annealing conditions might involve oxygen diffusion through the oxide layer, and/or the formation of oxygen interstitials or vacancies in the host. These defects can serve as charge trapping centers, causing device performance degradation and eventual failure.

To unravel this problem, we performed a systematic DFT study of different possible point defects in 9 lowest energy crystallographic phases of HfO₂ (Figure 2).

Deliverable D3.4

Impact of stable defect configurations on performances
and scaling of HfO₂-based Fe-devices

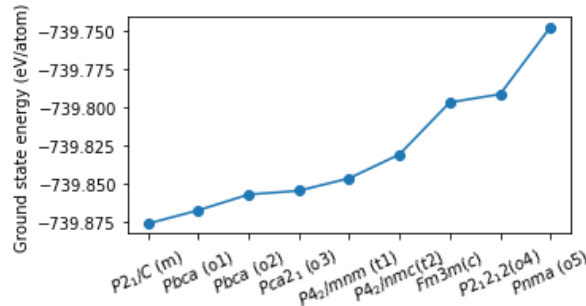


Figure 2. Difference in ground state energy with respect to monoclinic HfO₂.

The ground state energies of all the reaction products as well as reactants are calculated by solving the Schrödinger equation using density functional theory (DFT) within the generalized gradient approximation (GGA-PBE). Energy calculations of both ideal and defective hafnia crystal are performed in supercell with 96 atoms. A single point defect (vacancy or interstitial) is introduced in the supercell. Afterward the structures are relaxed in their various charge states using the geometry optimization scheme. This step is necessary as a defective crystal undergoes a structural change every time the defect acquires a charge. Finally, the ground state energy of the relaxed system is computed. A (2×2×2) Monkhorst-pack k-point mesh is used in the calculation.

Defect formation energy is computed as described in D2.3⁵ [1]:

$$\Delta E_{(V_X)/(X_i)} = \left\{ E \left[\text{HfO}_2^q_{(V_X)/(X_i)} \right] + q(E_V + E_F) \pm \mu_X \right\} - E[\text{HfO}_2] + E_{\text{Corr}},$$

where X={Hf, O}, and chemical potential of the constituent elements are bound to the growth conditions:

$$\mu_{\text{Hf}}^{\text{O-rich}} \leq \mu_{\text{Hf}} \leq \mu_{\text{Hf}}^{\text{Hf-rich}} \quad \text{and} \quad \mu_{\text{O}}^{\text{Hf-rich}} \leq \mu_{\text{O}} \leq \mu_{\text{O}}^{\text{O-rich}}.$$

Each defect can serve as a charge trapping center which can capture electrons/holes making the defects charged. A defect attains an equilibrium charge state for which the Gibbs free energy is minimum (ground state). Transition from charge state q_1 to q_2 can be attained by optical, thermal, or combined excitation. The external excitation can temporarily push the system out of equilibrium. The excess energy then gets dissipated into lattice heat (phonon) eventually bringing the system in thermal equilibrium with charge q_2 . To calculate the amount of energy lost in the relaxation process, we start from the ground state lattice structure (i.e., geometry optimized) of HfO₂ at q_1 . We include the q_2 charge and let the

⁵ <https://intersect-project.eu/wp-content/uploads/2022/04/D2.3.pdf>

system to relax. Relaxation energy is given by the difference between initial and the final energy of the geometry optimization process.

A thermodynamic transition between charge q_1 and q_2 occurs for the Fermi level value at which the formation energy of the two charge states is equal. Since it is an equilibrium phenomenon, the transition level is also called the *thermal transition level* E_{th} , is given by:

$$E_{th} = \frac{1}{q_2 - q_1} \left\{ E \left[HfO_2^{q_1}(V_X)/(X_i) \right] - E \left[HfO_2^{q_2}(V_X)/(X_i) \right] + E_v(q_1 - q_2) \right\}.$$

Table 1: Formation energy of different point defects in various crystallographic phases of HfO₂ at charge neutral state.

		Formation energy at zero charge (eV)				
		V _{O3}	V _{O4}	V _{Hf}	V _i	O _i
P2 ₁ /C (m)	Hf- rich	1.003	1.095	17.262	5.121	7.155
	O- rich	6.435	6.527	6.397	15.985	1.723
Pbca (o1)	Hf- rich	1.03	1.113	16.956	5.287	7.168
	O- rich	6.45	6.532	6.117	16.125	1.748
Pbca (o2)	Hf- rich	0.846	1.138	16.482	6.27	8.045
	O- rich	6.25	6.542	5.674	17.078	2.641
Pca2 ₁ (o3)	Hf- rich	0.861	1.098	17.043	8.304	7.046
	O- rich	6.261	6.498	6.243	19.104	1.646
P4 ₂ /mnm (t1)	Hf- rich		1.651	17.312	5.697	9.576
	O- rich		7.039	6.536	16.472	4.188
P4 ₂ /nmc (t2)	Hf- rich	0.803		17.19	4.436	6.5
	O- rich	6.167		6.461	15.165	1.136
Fm $\bar{3}$ m (c)	Hf- rich	0.856		16.264	8.177	6.31
	O- rich	6.169		5.638	18.803	0.997
P2 ₁ 2 ₁ 2 (o4)	Hf- rich	-1.637	-3.318	12.887	3.089	0.95
	O- rich	3.668	1.988	2.276	13.7	-4.356
Pnma (o5)	Hf- rich	0.182	0.299	15.768	10.133	7.724
	O- rich	5.421	5.538	5.29	20.612	2.484

Deliverable D3.4

Impact of stable defect configurations on performances
and scaling of HfO₂-based Fe-devices

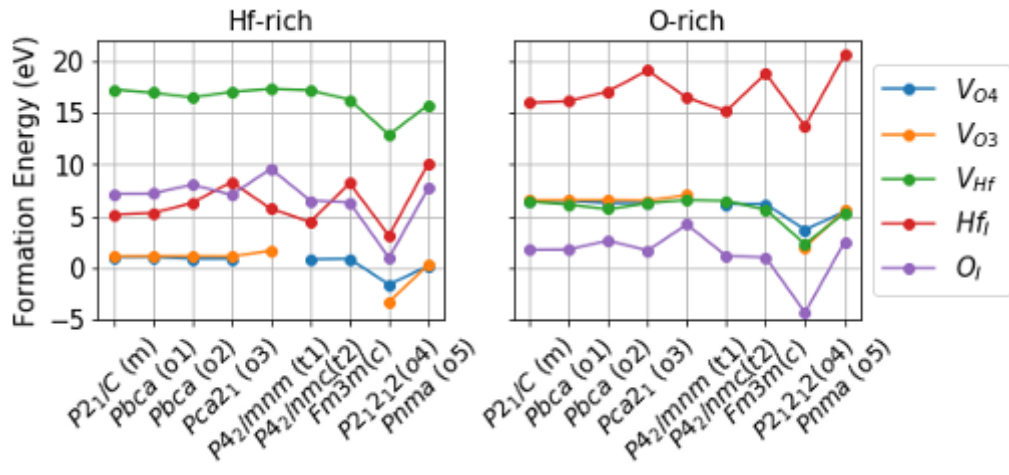


Figure 3. Comparison of the formation energy of various defects at their neutral charge state.

Table I and Figure 3 summarize the formation energy obtained in our calculations for all five possible types of point defects (namely O/Hf vacancies and interstitials) in their charge neutral state. They are given for two limits of the chemical potentials (Hf-rich and O-rich) and for nine crystallographic phases of HfO₂ under study.

The charge transition sequence ($q_1 \rightarrow q_2$) is calculated by finding the charge state for which Gibbs free energy is minimum at each Fermi level. For example, by increasing Fermi level V_{O3} defect of monoclinic goes in the sequence '+2' \rightarrow '0' \rightarrow '-1' \rightarrow '-2' charge state, while the state '+1' is not thermodynamically stable. Relaxation energy for such transitions for each of the phases as well as defects are listed in Table II.

Table II. Relaxation energy (in eV) of different point defects in various crystallographic phases of HfO₂ when it jumps from charge state q_1 to q_2 .

	Relaxation Energy (eV)						
	q_1	q_2	V_{O3}	V_{O4}	V_{Hf}	V_i	O_i
P2 ₁ /C (m)	2	0	2.0166	2.5001	0.0846		
	2	1				0.2605	0.9014
	1	0				0.2571	0.8431
	0	-1	0.0181	0.0737	0.0186	0.1916	
	0	-2					5.9645
	-1	-2	0.1527	0.1263	0.0206	0.1567	
Pbca (o1)	2	0	2.0003	2.5044			
	1	0				0.2455	0.3882
	0	-1		0.1597	0.019	0.0111	
	0	-2	0.3742				6.0062

	-1	-2		0.1957	0.0206	0.1890	
Pbca (o2)	2	0	2.0145	2.3472		1.4267	
	2	-1			3.2743		
	0	-1		0.0539			
	0	-2	0.5046			0.0399	6.7969
	-1	-2		0.1365	0.1374		
Pca2 ₁ (o3)	2	0	2.0812	2.4177			
	1	-2			6.5677	0.3434	
	0	-2	0.9363	0.7014			6.4934
P4 ₂ /mm (t1)	2	0	1.9304			1.0615	
	0	-1	0.0289			0.0167	0.5685
	-1	-2	0.0579		0.0115	0.0154	0.4883
P4 ₂ /nmc (t2)	2	0		2.5407		1.7267	
	1	-2					6.6847
	0	-1			0.0188		
	0	-2		1.3623		2.3875	
	-1	-2			0.0282		
Fm $\bar{3}$ m (c)	2	1					2.9974
	2	0		0.0168			
	2	-1				2.2316	
	1	-2					7.7920
	0	-2		4.255			
	-1	-2				2.7716	
P2 ₁ 2 ₁ 2 (o4)	2	0	2.7473				
	2	-1				1.9021	
	0	-2	0.7874	0.5369			6.1114
	-1	-2			0.2003	0.2203	
Pnma (o5)	2	0	1.5489	1.8347			
	0	-1	0.0118	0.0107	0.0055		
	0	-2					0.0443
	-1	-2	0.0113	0.0117	0.0076		

Unlike the defect concentration that depends on the formation energy, the thermal transition levels of the point defects are independent of the chemical environment (Hf/O-rich). These levels are experimentally measurable. In the lower energy allotropes, i.e., from monoclinic to cubic phases, attributed to the oxygen vacancies are located above the mid-gap while that for interstitial oxygen is located below mid-gap. In addition, the E_{th} of oxygen vacancies shows relatively small variation among different phases compared to other defects. E_{th} for V_{O4} is located between 0.5-2.0 eV below the conduction band minimum (CBM), and the same for V_{O3} that is at 0.25-1.5 eV below CBM. For the metal defects, E_{th} from V_{Hf} is located either below the valence band maximum (VBM) or outside of the bandgap. E_{th} for Hf_i is above the VBM, except for the FE o3-phase for which it is below the mid-gap. The

transition energies for both Hf_i and O_i interstitials are close to each other (trap depth are 2.71 eV and 3.13 eV, respectively).

GGA-DFT usually underestimates the experimental bandgap energy (E_g) of the materials, here are the computed values for all crystalline phases of HfO₂ under investigation (Table III). The main electronic properties and defects parameters are thus used for the device modelling described below (Sec. 4).

Table III. PBE computed bandgap (eV) of HfO₂ allotropes under study.

Allotrope	P21/C (m)	Pbca (o1)	Pbca (o2)	Pca21 (o3)	P42/mnm (t1)	P42/nmc (t2)	Fm3m (c)	P21212 (o4)	Pnma (o5)
E_g (eV)	4.214	4.251	4.315	4.484	4.177	5.047	4.465	3.937	3.776

3.2 Modeling TiN/HfO₂ nanocapacitor

3.2.1 System setup

Another relevant aspect in the characterization of the FE devices is the formation of the interface with the metal contacts. Thus, to model the properties of HfO₂-based devices and the effect of oxygen vacancy defects we have created a closed-circuit nanocapacitor with TiN electrode and HfO₂ slab as a dielectric. The system is simulated by using a periodically repeated supercells. A (1x1) periodicity of the supercell perpendicular to the interface is assumed. This setup gives the electrical short-circuit condition as well as an a realistic model of the electrode/perovskite super-lattice geometry.

We used a TiN slab of (10.47x15.03x9.71) Å³ as an electrode with an applied strain of 2%. The metal slab was symmetrically terminated with N atoms and contained 220 atoms. This corresponds to 4.5 unit cells along the (111) direction. For the dielectric part, the most stable polar orthorhombic phase of HfO₂ has been used. A symmetrically oxygen-terminated slab contained 312 atoms was considered for calculations. The thickness of the slab was 20.9 Å, which corresponded to 8 atomic layers, or 7.5 unit cells. Overall, the HfO₂/TiN nanocapacitor system contained 532 atoms, among them N_{Hf}=96, N_O=216, N_{Ti}=100, N_N=120 atoms, and had the dimensions of (10.47 x 15.03 x 34.88) Å³.

By using sequential variation of the interfacial distances at both sides of the dielectric we identified the most stable configuration and further performed full structural relaxation of the system preserving the lateral strain. We carried out first principles calculations with the PBE GGA density functional, as implemented in the SIESTA code. Psml-type of pseudopotentials and optimized basis set has been used for optimal performance. A 800 Ry mesh cutoff together with (3x2x1) k-points Monkhorst-Pack mesh have been used for calculations. The convergence of the total energy and forces per atoms were 0.001 eV and 0.02 eV/Å, respectively.

The lateral components of the lattice vectors were fixed at their values, while lattice in polar direction and atomic positions were optimized during geometry relaxation. The convergence of the total energy and forces during optimisation was of 1 meV and 0.01 eV/Å, respectively.

3.2.2 Properties of ideal HfO₂/TiN short-circuited nanocapacitor

The cell dimension of fully relaxed system is (10.47 x 15.03 x 35.785) Å³. Overall, the system is characterized by a strong rearrangement of two nearest layers in vicinity of the interface (Figure 4). Interfacial Ti atoms exhibit 0.9-1.0 Å displacements towards the interface, while the hafnia is partly disordered at the interface. Notably, the structure of the hafnia slab after relaxation does not show atomic displacements that could reduce its [001] polarization direction. The direction of polarization in our system is from P^+ to P^- , which are interfaces with smaller and larger values of Z-coordinate, respectively.

Despite the symmetric termination of both TiN and HfO₂ slabs, there is a symmetry breaking in the interfacial system due to the electrostatic conditions. Indeed, the length of formed interfacial N-O bonds at P^+ and P^- interfaces vary as 1.34 Å and 1.46 Å, respectively. Similarly, the Hf-O distances are varying as 2.12-2.29 Å for the P^+ and 2.14-2.26 Å for P^- interfaces.

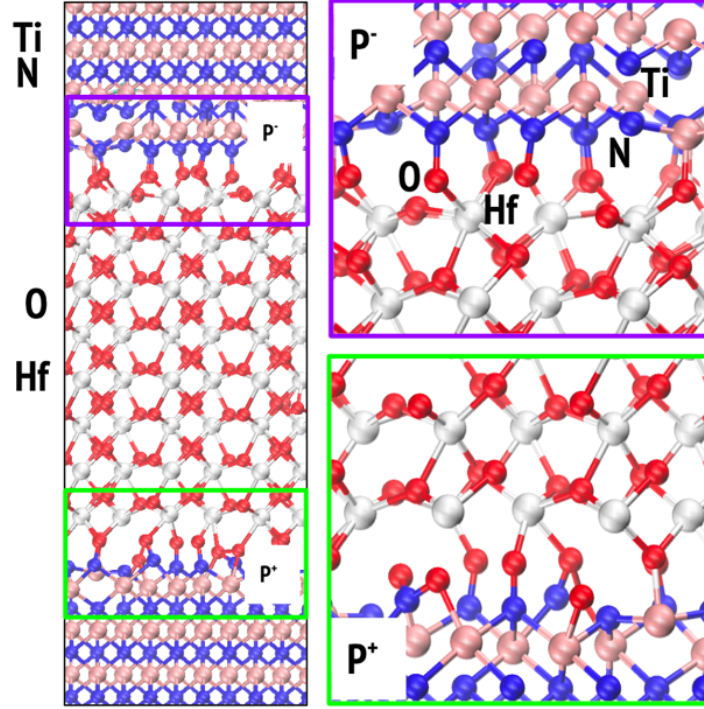


Figure 4. Relaxed structure of HfO₂/TiN system. Ti, N, O and Hf atoms are shown as pink, blue, red and gray spheres, respectively. Interfaces P⁺ and P⁻, marked as green and magenta rectangles are shown at the right side.

3.2.3 Electrostatic potential

To analyze the electrostatic potential across the system we constructed the planar and macroscopically average of electrostatic potentials of the TiN/HfO₂ system. The planar averaged potential was calculated across the capacitor as:

$$V(z) = 1/S_{xy} \int \int V(x, y, z) dx dy,$$

where $V(x, y, z)$ is three-dimensional electrostatic potential resulting from DFT calculations, S_{xy} is the cross-section of the slab. The planar averaged potential, $V(z)$, exhibits fast oscillations correlated with the atomic arrangement in the material. In order to take the information related to interfaces we have used a macroscopically averaged potential (MAV):

$$\langle V(z) \rangle = \int V(z) H(z - z') dz',$$

where $H(z)$ is the Heaviside step-function taken with the half period of the hafnia lattice parameter. The behavior of the MAV exhibits planar behavior in the electrode, while showing large amplitude oscillations at the interfaces P⁺ and P⁻, which are due to the

formation of interfacial dipoles. The potential drop (dE_1) between the electrode and P^+ interface is of 3.12 eV. The MAV across the hafnia slab shows a relatively small slope with the potential drop $dE_1 = 0.33$ eV (Figure 5). The latter is due to an imperfect screening from the metallic electrode, which is probably too thin in our simulations. We assume that the nature of potential slope is entirely related to interfacial phenomena and formation of chemical bonds at the interfaces between hafnia and electrode.

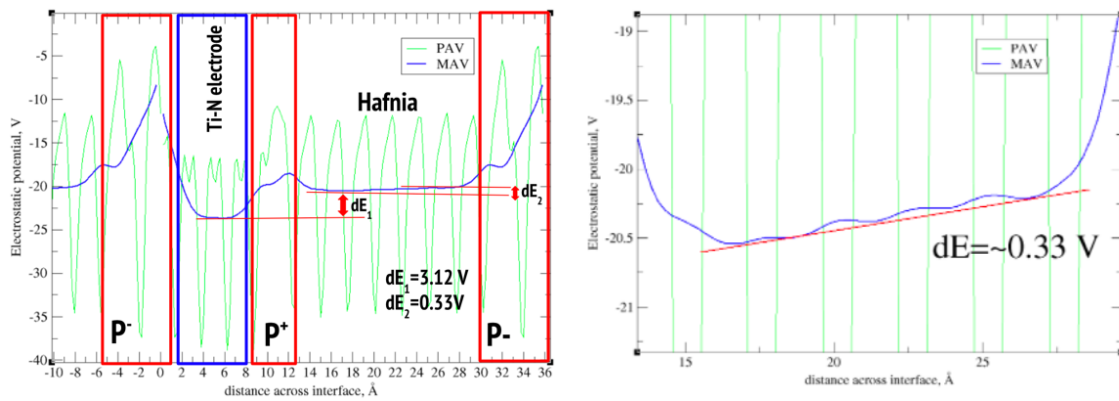


Figure 5. Planar (green solid line) and macroscopic (blue solid line) average of electrostatic potential in HfO₂/TiN nanocapacitor.

The band offset at the metal/ferroelectric interface was calculated using a spatially resolved projected density of states (PDOS) by defining the location of the band edges deep in the insulating region:

$$\rho(i, E) = \sum_{nk} \int_B Z \langle i | \psi_{nk} \rangle|^2 \delta(E - E_{nk}) dk,$$

where $|i\rangle$ is a normalized function localized in space around the region of interest (in our case, determined by the atomic orbitals basis set), and $\rho(r, E)$ is the local density of states.

We have constructed the atomic layers projected density of states for each atomic layer at Z-coordinate in the system. The TiN electrode represented, with 8 atomic layers corresponding to Ti and N states, exhibits a typical metal behavior with states crossing the Fermi level (Figure 6, black lines). Meanwhile the hafnia slab, represented by 8 atomic layers, shows a distinctive O and Hf states separation (Figure 6, red and blue lines for oxygen and hafnium atoms, respectively). Similarly to the bulk hafnia the top of the valence band is formed by oxygen states, while bottom of conduction band is formed by Hf states. The hafnia part of the constructed nanocapacitor does not exhibit any defect levels except for two layers in the

vicinity of the interfaces P^+ and P^- . Interfacial layers due to the strong structural relaxation have metallic character.

The bands of the hafnia slab show bending, i.e. the edges of the last occupied oxygen states are shifting while moving from P^+ to P^- . This is in agreement with observed behavior of electrostatic potential and appearance of a small but finite electric field in the system.

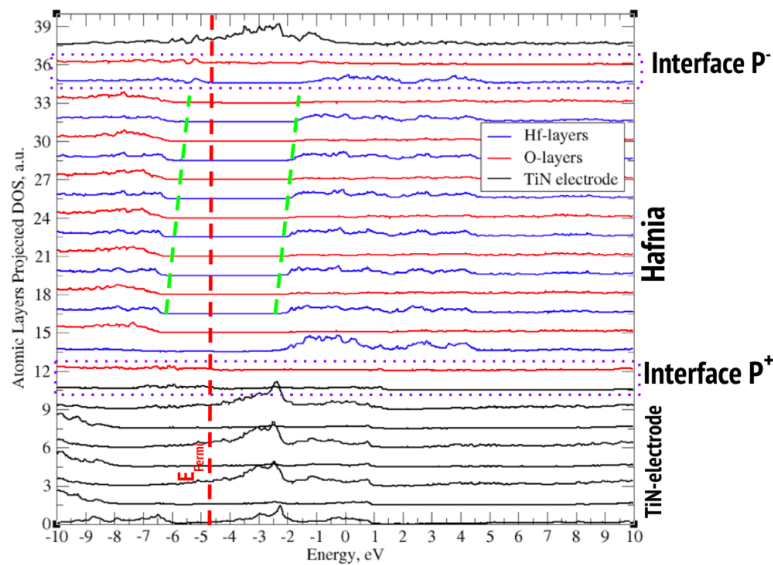


Figure 6. Atomic layers projected density of states for HfO₂/TiN nanocapacitor. Black lines correspond to TiN states, red and blue to Oxygen and Hafnium, respectively. Interfacial layers, P^+ and P^- , are partly disordered and exhibit metallic nature. Hafnia states show band bending with the edge of the occupied oxygen states following a green broken line.

3.2.4 Formation of Oxygen vacancies

In order to have a more realistic picture of the metal/hafnia interface, we considered the effect due to the presence of neutral O vacancies in the nanocapacitor. The creation of a neutral oxygen vacancy (V_o) in an oxide system corresponds to the appearance of two unsaturated electrons from cations. The orthorhombic phase of hafnia is characterized by 3- and 4-coordinated oxygen atoms. The calculation on bulk materials (Table I, Sec. 3.1) have shown a slightly different formation energy between both vacancies formed at both sites, with a slightly lower value for the 3-coordinated vacancy. However, the stability of the V_o vacancies in the polar system could be affected by the electric field across the system.

To consider both effects we have created ten vacancy sites (V_o^1 - V_o^{10}) with different coordinates along the polar axis. In addition, the different coordination of the host site has been considered, as in our sample sets we have: two vacancy sites at the interface in contact with the electrode, three 4-coordinated sites, and five 3-coordinated sites. Figure 7 shows the location of the vacancy sites and their coordination.

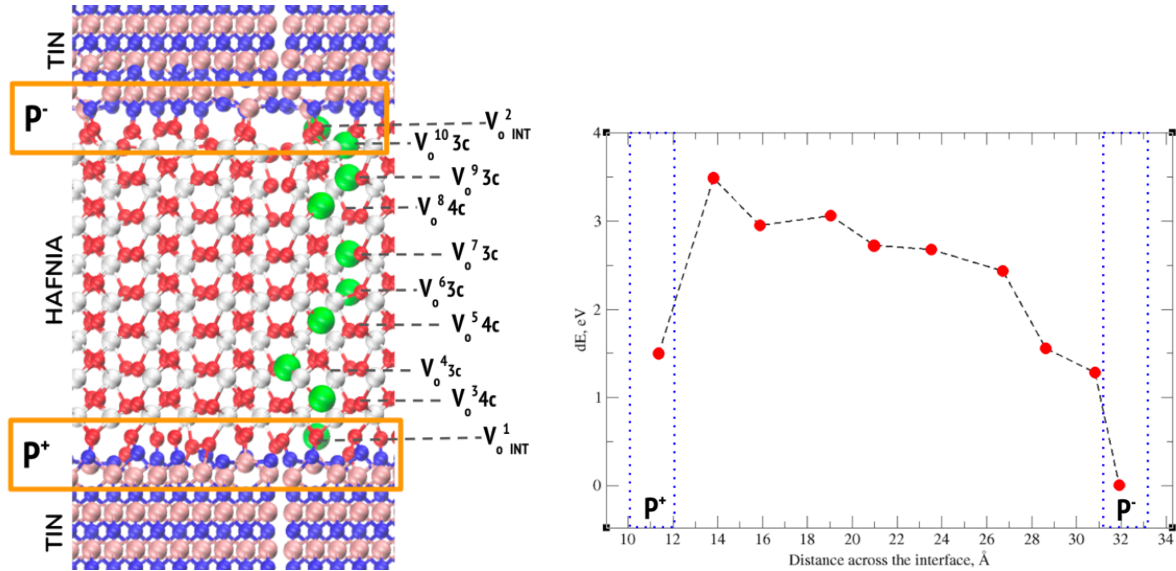


Figure 7. (left) Model of HfO_2/TiN nanocapacitor with neutral oxygen vacancy sites (V_o). Several sites across the system ($V_o^1 - V_o^{10}$) and different coordination, 3 coordinated (3c) and 4 coordinated (4c), have been sampled. (right) Relative vacancy stability along the polar axis showed preferred configuration at P^- interface.

Initial configurations with the vacancy sites were relaxed at fixed lattice, by using 800 Ry mesh cutoff, (3x2x1) k-points Monkhorst-Pack mesh. The convergence of the total energy and forces per atom were 0.001 eV and 0.02 eV/Å, respectively. The outcome results demonstrate that structural relaxation around the vacancy sites involves only a few neighboring shells making the hafnia matrix resilient to the vacancy formation. The analysis of electronic properties demonstrate that location of V_o defects at the interfacial layers (P^+ and P^-) leads to the lowering of the CBM for hafnium atoms in the vicinity of the interface. This effectively increases the dead-layer, reducing the thickness of active FE materials.

The analysis of MAV electrostatic potential demonstrates local perturbation of the potential caused by the presence of the vacancy defect. However, the overall MAV potential slope is preserved similar to the non-defective capacitor system. Remarkably, our results indicate that the formation of V_o defects in HfO_2/TiN capacitor is mostly energetically favorable at the interfacial regions. Due to electrostatic conditions in the system the relative stability (dE) of V_o defects in hafnia exhibits an ascending trend towards P^- interface: the most stable vacancy site is at the P^- interface. Such a trend implies that, due to thermal hopping between nearest sites, oxygen vacancies will preferably accumulate at the P^- interface.

Since the charge balance at the P^- and P^+ sides is crucial for defining the dipole across the FE material, the diffusion of oxygen vacancy defects plays an important role for overall

performance of HfO₂-based FE devices. The diffusion barriers for V_O defects in hafnia to define a safe operating temperature interval where vacancy diffusion will be reduced. In addition, the consideration of charged defects, and their dynamics might be another mechanism contributing to screening properties of hafnia.

4. DFT-based Ferroelectric Device Simulations

4.1 Ginestra® Ferroelectric Model

The physics of ferroelectric materials is modeled using the Poisson-Ginzburg-Landau model (PGL) that describes the Landau free-energy in proximity of a phase transition. According to the model, the dielectric polarization is governed by the Landau-Ginzburg dynamic equation:

$$\rho_v \frac{d\mathbf{P}}{dt} + \nabla_P u = 0,$$

where the viscosity ρ_v [Ωm] is a damping constant that corresponds to the internal resistivity of the ferroelectric, which limits the changes of the polarization with time. The Landau free energy u is given by:

$$u = \alpha \mathbf{P}^2 + \beta \mathbf{P}^4 + \gamma \mathbf{P}^6 + g(\nabla \mathbf{P})^2 - \mathbf{F} \cdot \mathbf{P} - \frac{\epsilon_0 \epsilon_r}{2} \mathbf{F}^2.$$

Here, α , β and γ are the ferroelectric anisotropy constants and \mathbf{F} is the electric field in the ferroelectric material. The latter Equation is coupled to the Poisson's equation to provide \mathbf{F} and \mathbf{P} within the FE-device. Below T_C , one has: $\alpha < 0$, $\beta > 0$ and $\gamma = 0$ for second-order phase transitions, or $\alpha < 0$, $\beta < 0$ and $\gamma > 0$ for first-order phase transitions. The α parameter depends on the temperature according to:

$$\alpha(T) = \alpha + \alpha_T(T - T_C),$$

where T_C is the Curie temperature.

4.2 FE Simulations: Results and Discussion

The FE model described in the previous Section has been used to evaluate the impact of material and trap properties on ferroelectric switching dynamics, charge trapping effects and device reliability. The modeling framework couples the FE model with charge (e/h), and

material transport as well as with stress-induced material modifications. All of these are critical to model device aging and the reliability phenomena as well as physics behind it. The capability to handle discrete contributions of charge, atomic species, and defects (i.e. interstitial ions and vacancies) is included, as well as the capability to simulate their diffusion and generation processes. The results of DFT calculations described in Section 3 are taken as inputs to the device simulations. As a case study, we focus on Zr-doped FE-HfO films (HZO).

4.2.1 Device simulation approach

Given the polycrystalline nature of FE HZO films, we simulated FE capacitor and FeFET devices comprising a multi-grain FE layer similar to the one depicted in Figure 8a. O-vacancy rich grain boundaries (GBs) separate the HZO grains with different phases – monoclinic (m), tetragonal (t), and FE and non-FE orthorhombic (o) – and properties (bandgap, different preferential direction of domain growth, k-values, defect energies) that altogether result in different distribution of coercive field (E_c) and remanent polarization (P_r), see Figure 8b. The main material and defect properties (thermal ionization energies, vacancy relaxation energies and bandgap) calculated using DFT methods (Tables I-III) have been used as input in the device simulations. They are essential to study the switching-trapping interaction that are responsible for several key reliability aspects, such as imprint, wake-up and variability.

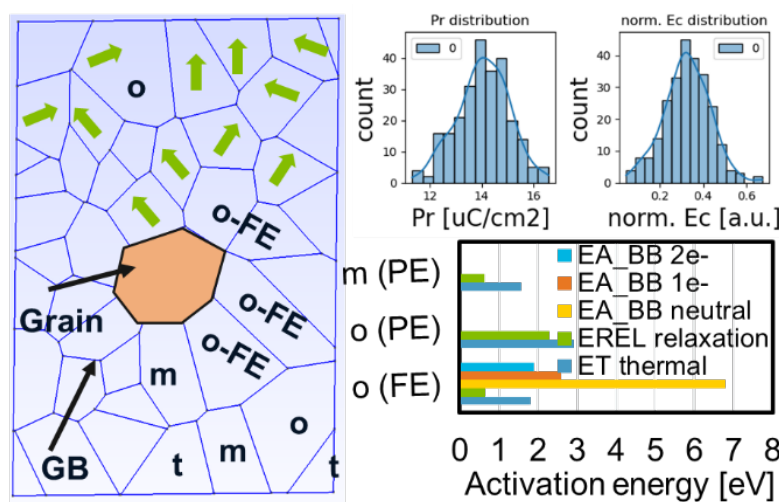


Figure 8. (a) Polycrystalline/ multiphase nature of FE, (b) P_r and E_c distribution of HfO FE.

4.2.2 Charge trapping effect on ferroelectric switching hysteresis and speed

To study the interplay between ferroelectric switching and charge trapping at defect sites, we first calibrated the FE model by reproducing an experimental polarization-voltage (P-V) cycle, Figure 9a, and then performed FE switching simulations while accounting for the material and defect properties calculated using DFT methods (see Section 3).

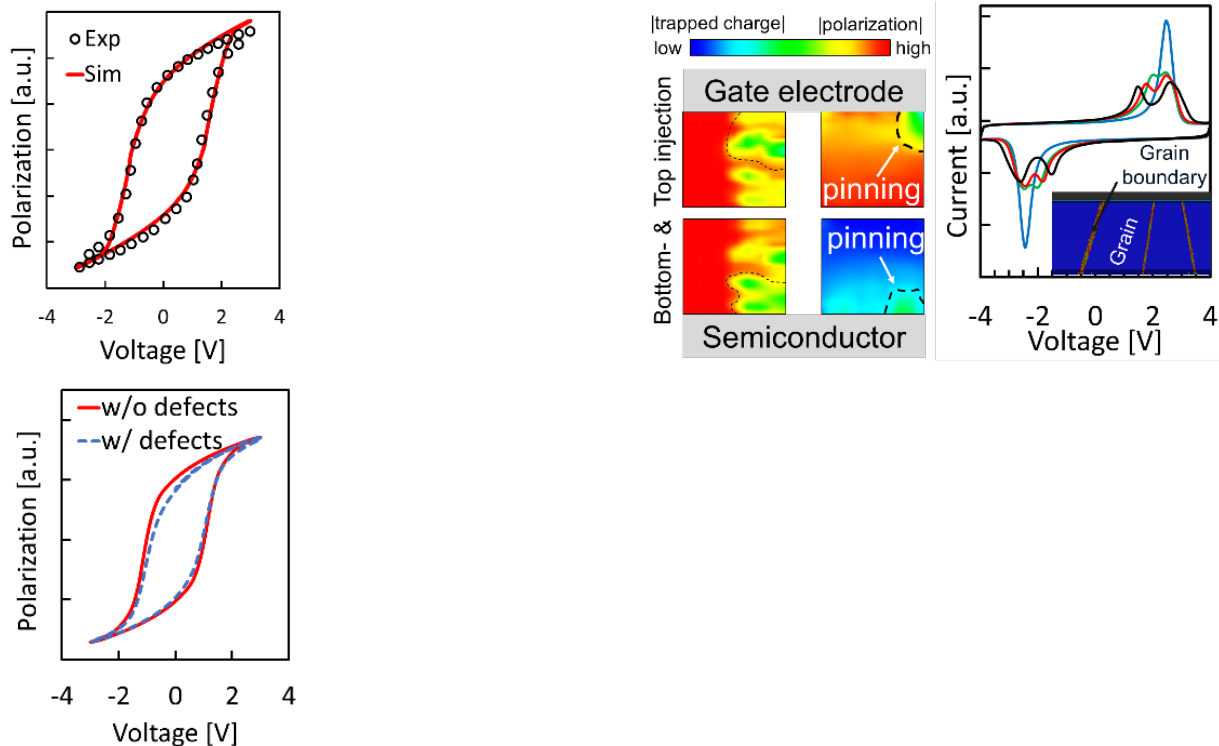


Figure 9. (a) calibrated metal-ferroelectric-metal (MFM) capacitor using developed multi-grain FE model within Ginestra®. Interaction of electronic charge and FE switching and its impact on: (b) domain pinning; (c) deformation of the hysteresis (wake-up) through trapping on grain boundaries (GBs) of polycrystalline HfO_x; (d) Pr fluctuation.

The simulation results highlight multiple effects induced by electron injection and consequent trapping at defects and GBs leading to alteration of device electrostatics: (i) impact on switching kinetics and E_c ; (ii) pinning of the FE domain and switching OFF a portion of the device resulting in smaller P_r (Figure 9b); (iii) creation of local internal fields and deformation of switching current and remnant polarization, Figures 9c-d.

4.2.3 Impact of HfO_x traps on domain nucleation and variability

Among the many technologies that have been proposed for the hardware implementation of artificial neurons and synapses in neural networks, ferroelectric devices are among the most promising. Beside the two terminal ferroelectric tunnel junctions (FTJs) - predominantly envisioned for crossbar applications and artificial synapses [2-4]- both artificial neuron and artificial synaptic behavior have been demonstrated in FeFET [5-10]. One of the key interactions to be captured and understood in engineering FE devices for neuromorphic applications is the interplay of FE switching and charge trapping.

Here, we focus on defect-domain interactions and on the impact of defects on domain nucleation and device variability, by simulating ferroelectric switching dynamics of a FTJ device operated under the application of a sequence of identical pulses (as typically done for neuromorphic applications). Simulated devices were created accounting for material properties and oxygen vacancy defects [Figure 10a], as calculated with DFT in Section 3. Simulations show that upon the application of the initial voltage pulses, electrons are trapped at the defect sites, causing perturbations in the electric field that initiate domains nucleation (Figure 10b). The application of additional voltage pulses results in the coalescence of the nucleation sites into large domains, Figure 10c-e, eventually covering the whole switchable portion of the device. It is this gradual nucleation process, together with the plurality of FE domains and distribution of coercive field and remnant polarization values, that can be exploited for the multi-level operation required by neuromorphic applications.

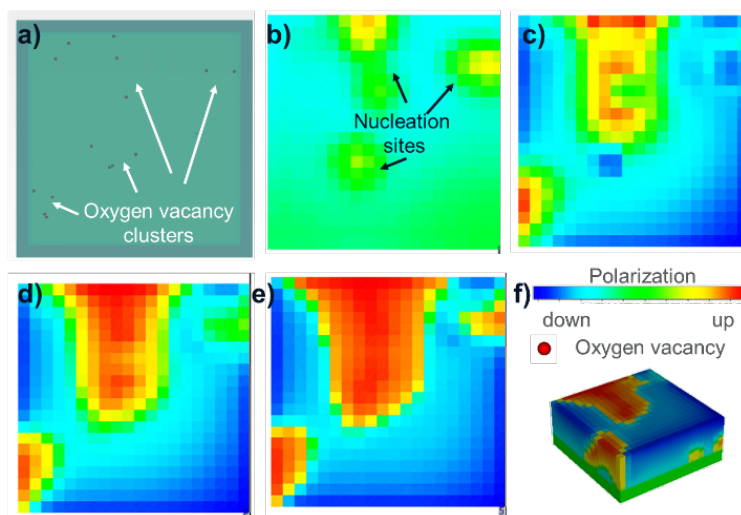


Figure 10. Domain nucleation. a) top view of the FTJ with oxygen vacancy clusters. b) – e) nucleation of the domain with time starting from the local perturbation at the defect. f) 3D view of the domain configuration at case e) together with the legend.

However, the same aspects enabling a gradual FE switching discussed above – especially the distribution of E_c and P_r – are also responsible of device-to-device variability, which must be kept under control to guarantee good neuromorphic operation.

We thus used simulations to investigate variability and its dependence on the device size, which determines the number of available switching domains. Results highlight two main aspects:

- the device scaling and the consequent reduction of domains number results in a larger variability of the ON-state current, Figure 11a
- the OFF-state current also shows a larger variability. In fact, by reducing the device size, also the number of the O vacancies within the FE material is reduced. Since these vacancies are the ones supporting the OFF-state trap-assisted tunneling current, their

larger variation in energy and space position leads to an overall larger variability of the OFF-state current, Figure 11b.

Our simulation results clearly indicate a trade-off between the device size, the variability and the number of domains required for the analog switching is observable. Given the average domain diameter of 10 nm, (using modelling) we determined that a minimum size of at least 64 domains (or cell size of 80nm x 80nm) is required for the smooth potentiation and depression operations shown in Figure 11c.

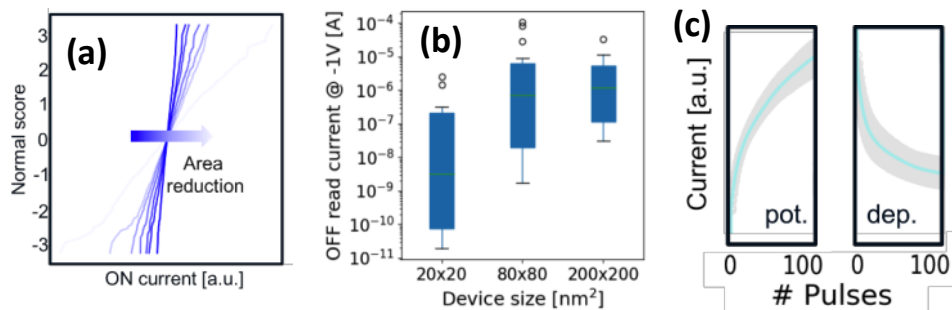


Figure 11. (a) ON current variability relaxation with area increase. (b) OFF current variability relaxation with cell area increase. (c) Optimized 80x80nm FTJ potentiation (left) and depression (right) characteristics.

4.3 FeFET modelling

The displacement-current/voltage characteristics of the FeFET are simulated by using the Ginestra® modeling platform utilizing a 1D metal-ferroelectric-insulator-semiconductor (MFIS) structure (Figure 12a) with a Preisach model for ferroelectric HfO₂ with a remnant polarization of $\pm 15 \mu\text{C}/\text{cm}^2$. The applied voltage hysteresis waveform for the simulation shown is in Figure 12b. The output current as well as the charge due to dielectric and ferroelectric response are shown in Figures 12c-d, respectively. During the upsweep from 0V to 5V a ferroelectric polarization is switched, but during the down-sweep the ferroelectric polarization depolarizes back, due to a formation of depolarization field over the HfO₂ layer. Almost no polarization can be stabilized with a MFIS structure and only $2 \mu\text{C}/\text{cm}^2$ remain once the voltage returns to 0V. This is below 10% of the total ferroelectric polarization charge density. To maintain a stable retention and a percolation path between source and drain in the ferroelectric transistor, ideally all domains/dipoles in the ferroelectric HfO₂ should be pointing in one direction.

Deliverable D3.4

Impact of stable defect configurations on performances and scaling of HfO₂-based Fe-devices

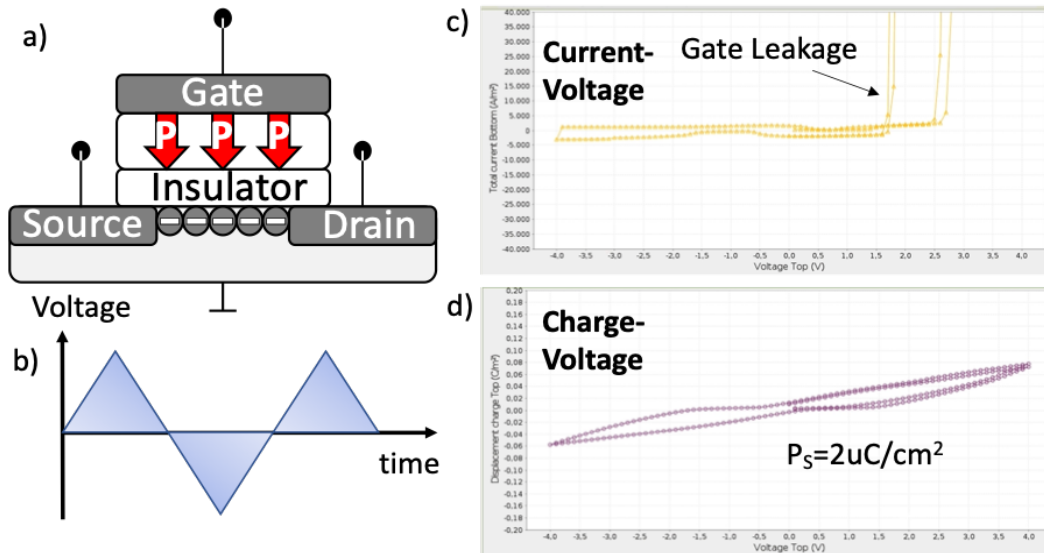


Figure 12. a) Sketch of the FeFET with the polarization bringing the channel in inversion b) Hysteresis waveform applied in Ginestra c) Current-voltage characteristic of the FeFET corresponding to the waveform in b), d) polarization and displacement charge-voltage characteristic of the FeFET.

To study the impact of defects on the ferroelectric switching process, the most common bulk defects in HfO₂, i.e., oxygen vacancies are included in the simulation (Sec. 3). The DFT calculated band gap and the optical transition energy from V^+ and V^{2-} state the for monoclinic HfO₂ phase have been used for the FeFET simulations. Hence, the defects with the energy levels corresponding to V^+ and V^{2-} for 3 different oxygen vacancy concentrations were added to the simulation as shown in Figure 13. With a moderate defect density of $3 \times 10^{19} \text{cm}^{-3}$, which can be found also in state-of-the-art HfO₂ gate dielectrics of logic FETs, almost no impact of the defect charge on the polarization switching can be found. In Figure 13b the defect density was increased by a factor of 3. Small ferroelectric switching peaks emerge. This can be attributed to screening of ferroelectric charge by defect charge that reduces the depolarization field inside the ferroelectric HfO₂ and allows for higher amount of stabilized polarization.

Deliverable D3.4

Impact of stable defect configurations on performances
and scaling of HfO₂-based Fe-devices

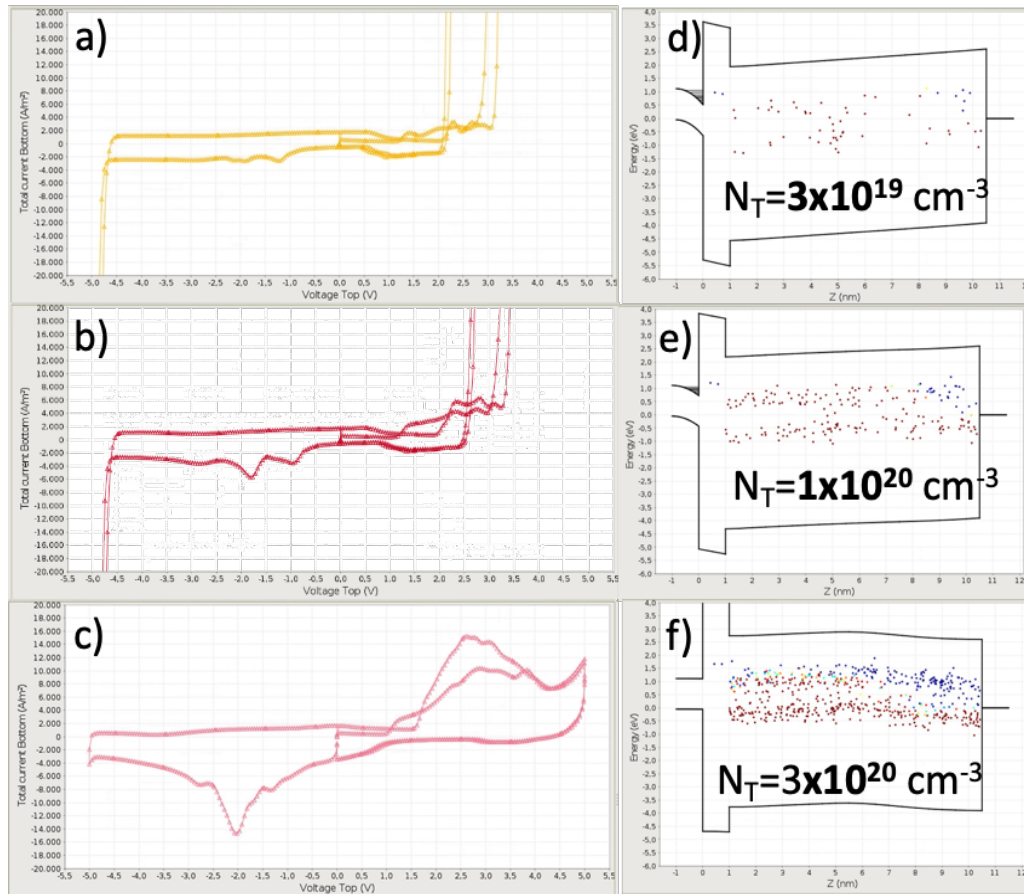


Figure 13 Current-charge characteristic of FeFET during hysteresis voltage sweep with a bulk trap density of a) $3 \times 10^{19} \text{ cm}^{-3}$ b) $1 \times 10^{20} \text{ cm}^{-3}$ and c) $3 \times 10^{20} \text{ cm}^{-3}$. Band diagram without gate bias after last positive triangular voltage sweep with a bulk trap density of d) $3 \times 10^{19} \text{ cm}^{-3}$, e) $1 \times 10^{20} \text{ cm}^{-3}$ and f) $3 \times 10^{20} \text{ cm}^{-3}$.

In order to achieve ferroelectric capacitor current responses similar to the experiment the trap density needs to be increased to $3 \times 10^{20} \text{ cm}^{-3}$, for both upper and lower trap band as shown in Figure 13c. Although the polarization can be completely switched, after the external voltage returns to 0V, the silicon substrate is in a flatband voltage condition (no net charge) and not in inversion as required for ferroelectric transistor device operation (Figure 13). To further study this behavior the band diagram and defect occupation from the simulation during program, erase operation and retention was analyzed in more detail for the oxygen vacancy density of $3 \times 10^{20} \text{ cm}^{-3}$.

During the program operation the FeFET undergoes a partial polarization switching together with electron trapping near the interface (the occupied traps are indicated as red circle in Figure 14). A further increase of the sweeping voltage to 5V invokes more switching and

trapping until the polarization charge is overcompensated by trapped charges. During the down sweep from 5V the reduction in the displacement current-voltage characteristic below the dielectric level can be attributed to the onset of silicon depletion in Figure 14. This allows us to determine the *threshold voltage* V_{TH} of around 3V, which also quantifies the amount of negative charge from filled oxygen vacancies. At 0V gate voltage (band diagram #3 in Figure 14b) trapped electrons close to the interface are already released and the FeFET is in a flatband voltage condition. This corresponds to a threshold voltage of ca. 1.5V.

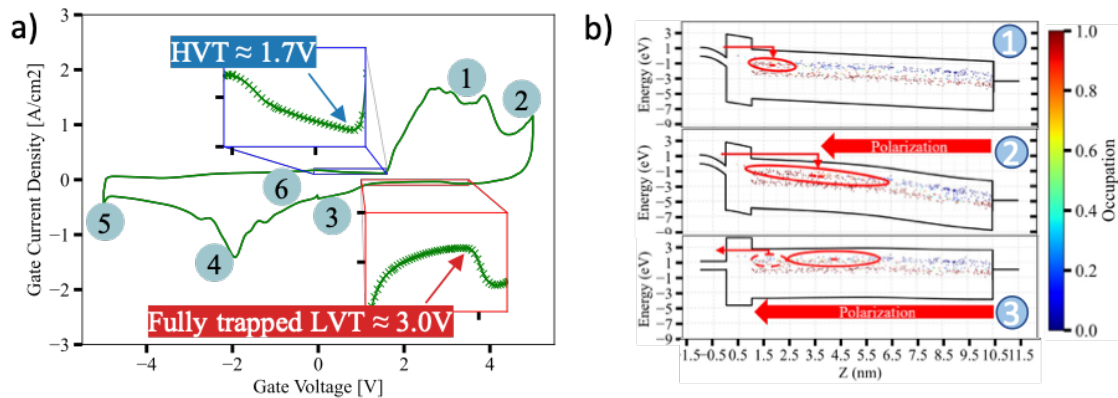


Figure 14 a) Displacement and ferroelectric current density during hysteresis sweep; b) band diagram under different applied gate voltages. Circles illustrate charge from trapped electrons and polarization is indicated by arrows. The numbers refer to the positions indicated in the I-V sweep in a).

By sweeping down to around the negative voltage, trapped electrons from the program operation will be released again. Only the electrons trapped at the center of the HfO₂ layer will remain (band diagram #4 in Figure 15b). Additionally, the lower trap band near the interface is emptied as well, creating positive charges to compensate for the remaining polarization. A further decrease in the applied voltage leads to further emptying of the lower trap band to compensate the polarization switching (band diagram #5 in Figure 15b). After sweeping back to 0V again, the trapped holes and electrons remain stable (band diagram #6 in Figure 15b) and the cell is in high V_{TH} (HVT) state.

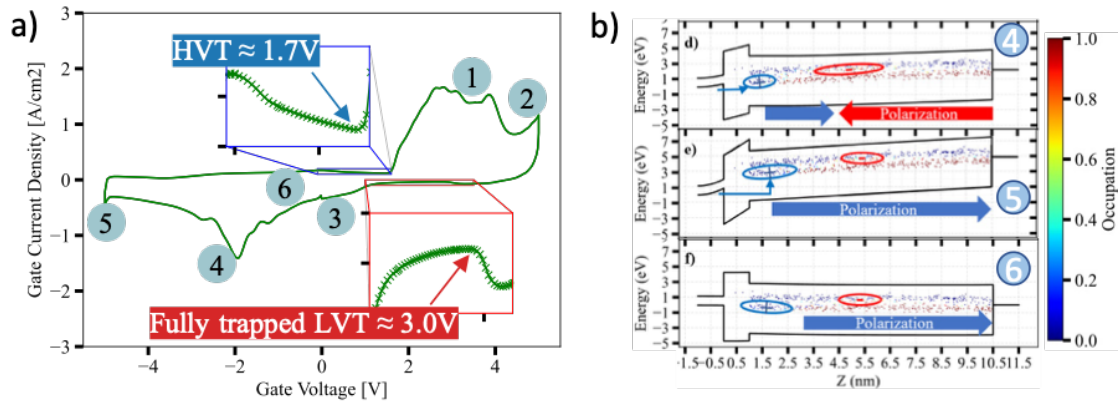


Figure 15 a) Displacement and ferroelectric current density during hysteresis sweep b) band diagram under different applied gate voltages. Circles illustrate charge from trapped electrons and polarization is indicated by arrows. The numbers refer to the positions indicated in the I-V sweep in a).

A retention simulation with 0V gate bias for 10 years of the FeFET with bulk trap density of $3 \times 10^{20} \text{ cm}^{-3}$ is performed to check the long-term stability of the polarization. Directly after the positive triangular gate sweep the polarization is overcompensated by negative charge from charged oxygen vacancy traps (Figure 16b) and or band diagram #3 in Figure 14b. This leads to a flatband condition (panel a) in the Silicon channel that is non-conductive. This is a non-functional state for the device, as Silicon channel should be in inversion and conduct electrons between source and drain after applying a positive write voltage. During the first second, electrons above the Fermi-energy are released to the channel or the transistor gate. This can be quantified by the flatband voltage shift of the FeFET due to trapping charge in Figure 16b. Since this negative charge is also responsible for stabilization of the polarization once the electrons are released, the polarization reduces as well. There is a time point where the positive polarization charge is higher than the negative trap charge and a polarization wedge structure is formed (Figure 16c). This pushes the upper trap level close to the SiO₂/HfO₂ interface below the Fermi-energy and the excess electrons in the middle of gate stack are not released to the Silicon channel or metal gate, but fill those stable trap states at the SiO₂/HfO₂ interface. After 1s both electron traps and polarization are stable for 10 years, which is crucial for non-volatile memories. The total flatband voltage shift is such that the Silicon channel is in inversion and electrons in the FeFET can be conducted from source to drain.

Deliverable D3.4

Impact of stable defect configurations on performances and scaling of HfO₂-based Fe-devices

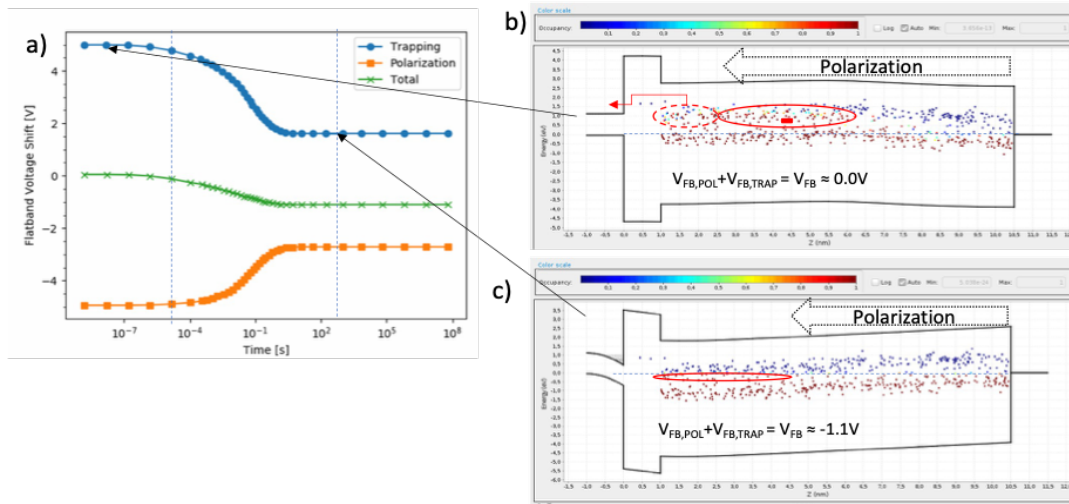


Figure 16. a) Flatband voltage shifts during retention time due to individual contribution of trapping and ferroelectric polarization as well as total shift. b) Band diagram 10us after positive triangular voltage pulse c) Band diagram 1000s after positive.

For neuromorphic computing as well as memory applications it is important that the channel is in inversion directly after the write operation. The simulation shows that a possible pathway to optimize the gate dielectrics and traps is, e.g., reducing the bulk trap density and increasing the trap density at the SiO₂/HfO₂ interface, with energy levels kept slightly below the Fermi-energy for the stable wedge structure. If the trap density can be optimized in such a way, so that the traps are filled with electrons with a remaining charge of $2\mu C/cm^2$ (polarization + charged defects), no electron detrapping process is required and the FeFET can be directly read-out after write operation.

5 Experimental data

Planar long channel FE-FETs were fabricated at IMEC with a gate first flow, with Si-doped HfO₂ and (5 nm) HZO stacks, deposited on thin oxide layers, with TiN metal gate electrodes, as displayed in the cross-section in Figure 17a. An undoped HfO₂/TiN stack, subjected to similar thermal budget as the Si-doped HfO₂ was included as a reference for the paraelectric nature of the HfO₂ structure. Each sample received an appropriate ferroelectric anneal, to attain the ferroelectric orthorhombic phase, as highlighted in the polarization-voltage curves in Figure 17b for the HZO and Si-doped HfO₂ sample [11].

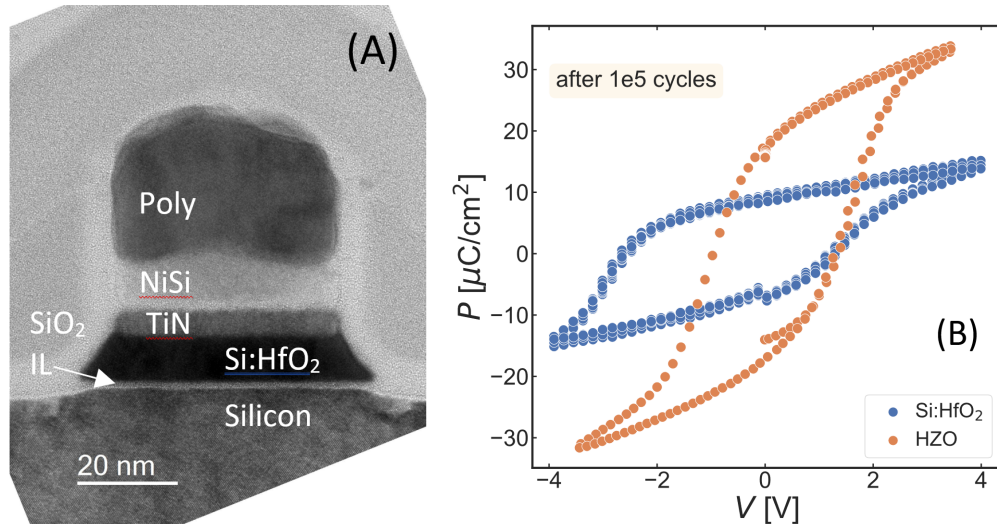


Figure 17. (a) Cross section Transmission Electron Micrograph of Si-doped FEFET sample with $\sim 9.5\text{nm}$ ferro layer on thin Silicon oxide interface layer. Note this example is of shorter channel device than that studied in this work. (b) shows example Polarisation-Voltage curves after 1×10^5 cycles, for the ferroelectric Si:HfO₂ and HZO layers examined in this study.

Charge trapping and emission properties were explored by monitoring the drain current (at $V_g = V_{th}$) intermittently during stress, and transforming to a threshold voltage shift with respect to the pre-stress device transfer characteristics at multiple temperatures, as illustrated in Figure 18a. In this case, the stress field was calculated as the ratio of overdrive voltage, normalized by the device equivalent oxide thickness (EOT), as derived from the analysis of capacitance-voltage characteristics (CVC). An example of ΔV_{th} as a function of emission time, at different electric field conditions for HZO is shown in Figure 18b. Note that these devices were not biased/polarized into either state prior to these measurements. At low electric fields, after short stress times as shown here, initially significant charge trapping is present, which is emitted during the subsequent relaxation phase. On increasing the bias, this continues until a maximum ΔV_{th} is seen (at 5 MV/cm), above which the ΔV_{th} reduces, and even relaxes to negative this continues, until a maximum ΔV_{th} is seen (at 5 MV/cm), above which the ΔV_{th} reduces and even relaxes to negative ΔV_{th} values, implying the commencement of the polarization switching of the structure to the low V_{th} state (following positive bias) during the measurement sequence. In this study its impact is limited by focusing on a single bias voltage, below which no negative ΔV_{th} is observed at any of the temperature ranges explored. For this, the $V_{ov} = V_g - V_{th0}$ value is 0.9V for HfO₂, 0.6V for Si:HfO₂ and $\sim 0.4\text{V}$ for HZO, yielding an effective electric field of 3 MV/cm for subsequent analysis.

The change in V_{th} with stress and emission times is shown for undoped HfO₂ (Figure 19), at temperatures between 77 and $\sim 400\text{K}$. Significant charge trapping and emission are present across all temperature ranges for the devices measured, and appear to show limited temperature activation. These datasets were modelled using the capture-emission map

Deliverable D3.4

Impact of stable defect configurations on performances
and scaling of HfO₂-based Fe-devices

methodology, employing non-radiative multi-phonon parameters describing capture in and emission from defects located in a specific number of sub-populations. In each case, the defect capture and emission activation energy values (E_{Ac} and E_{Ae} , respectively) are assumed to be normally distributed, and the capture and emission times (τ_c and τ_e , respectively) related to activation energy by the Arrhenius relationship.

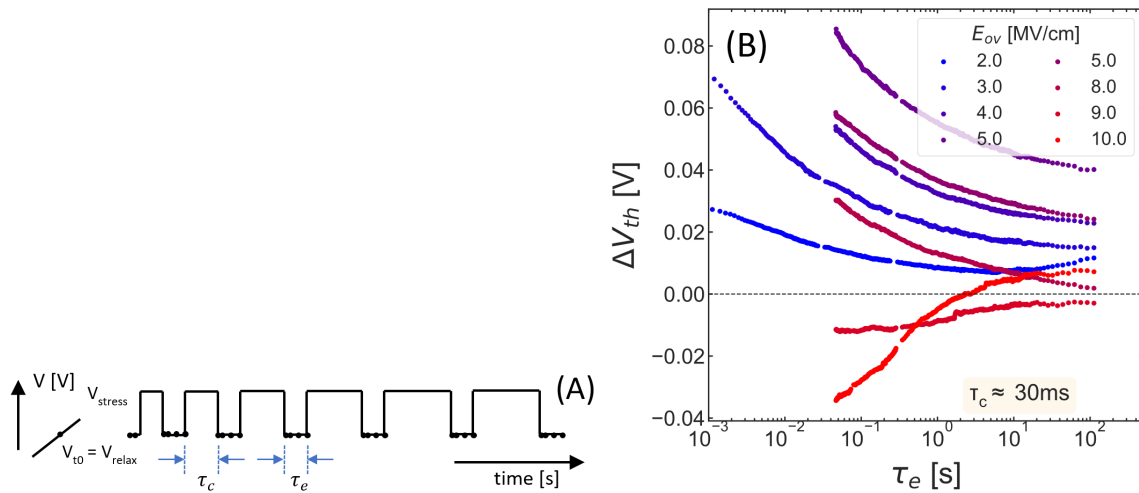


Figure 18. (a) Voltage sequence as applied in this work, while (b) shows ΔV_{th} as a function of emission time, at 25°C, after 30 ms stress for various bias conditions. Low bias response is consistent with electron emission, whereas partial polarisation of HZO ($\Delta V_{th} < 0$) is observed after stress bias conditions.

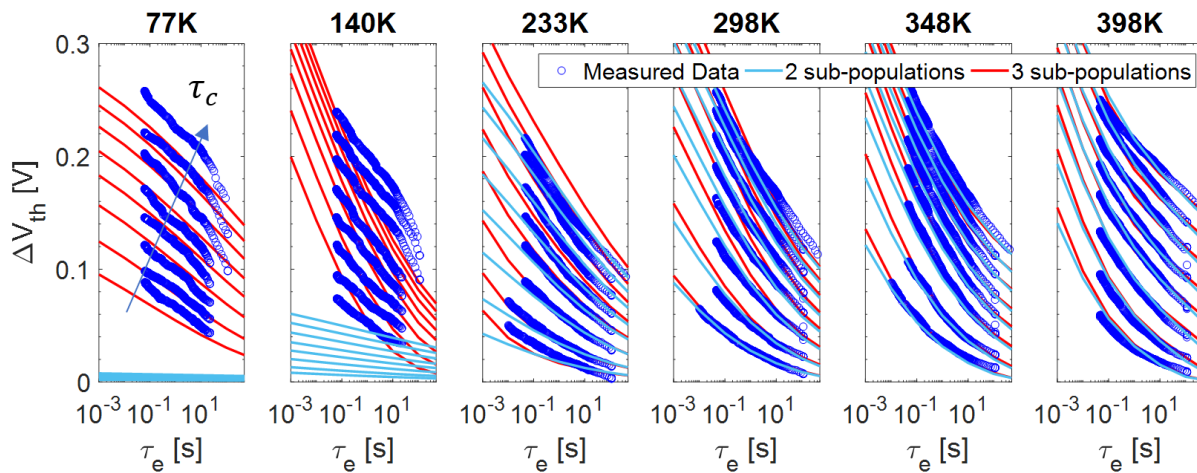


Figure 19. Measured and calculated ΔV_{th} shift, as a function of emission time, for capture times between 30ms and 2 ks, across a range of temperature conditions (blue symbols), for an undoped HfO₂ sample. Solid lines are fits of 2 defect subpopulations (R_1 and R_2), previously modelled on the 230-400K datasets show an excellent fit to these datasets, but clearly does not match the low temperature response, where their prediction of defect freezeout is not observed experimentally. Incorporating a third defect center R_3 yields a good fit across a wide temperature range.

In a bid to model the measured low-temperature response, an additional defect distribution, R_3 , was introduced. Fit parameters (E_{Ac} , $\sigma_{E_{Ac}}$, E_{Ae} , $\sigma_{E_{Ae}}$, τ_0 and ΔV_{th}) describing the defect ensemble were established on the low temperature datasets and combined with those values describing the higher temperature response. The aggregate of parameter sets of the three defect centers yields an excellent fit to the measured capture and emission dataset (Figure 19, red lines), across a temperature range exceeding 300K.

The parameter set optimized for the three defect centers in Figure 19 are represented in Figure 20 as an *activation energy map*, where the energy alignment of the three defect centers is displayed. Defect center R_1 , with median E_{Ac} and E_{Ae} values of ~ 1 eV implies it is located ~ 1 eV higher than the Fermi level in the silicon surface, so is not readily accessible, and plays a role at the longer stress times (and higher bias conditions, not explored here), while the defects R_2 and R_3 with median E_{Ac} and E_{Ae} values of ~ 0.5 and 0.2 eV are more easily accessed, and can play a stronger role at lower temperatures, and shorter stress times.

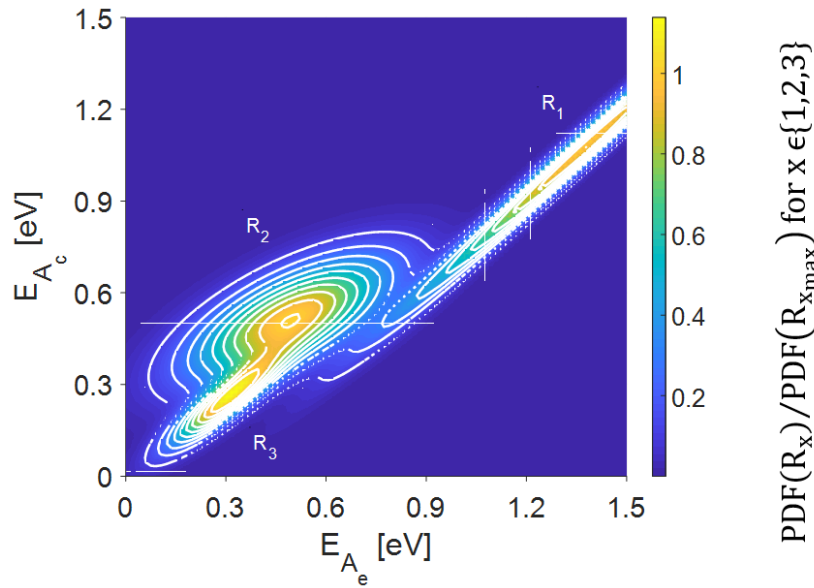


Figure 20. E_{Ac} - E_{Ae} map for undoped HfO₂, generated for measurements collected between 77 and ~ 400 K, showing three energy locations of the defect centers applied in the model in Fig. 3. Two of these defect centers (R_2 and R_3) have low E_{Ac} and E_{Ae} , and thus can contribute at low temperature and/or short time scales. Each defect center is normalized to its maximum value.

The results for all three samples demonstrate that significant charge trapping is possible in defects with very low activation energies (R_2 and particularly R_3), in paraelectric and ferroelectric HfO₂ layers. This implies their energy levels are very close to the silicon Fermi level, and therefore can readily contribute to sizeable V_{th} shifts. In the case of ferroelectric samples, V_{th} shifts as large as ~ 0.2 - 0.3 V can be attributed to R_2 and exceeding 0.5 V to R_3 sub-populations (Table IV). Using the Arrhenius equation for each sub-population (whose pre-

Deliverable D3.4

Impact of stable defect configurations on performances
and scaling of HfO₂-based Fe-devices

factor τ_0 determines the time/temperature at which they contribute), enables the temperature dependance of each to be decoupled, as a function of capture and emission time (τ_c and τ_e , respectively). Results for HfO₂, Si:HfO₂ and HZO layers, calculated at 398K, for τ_c and τ_e less than 1s are shown in Figure 21. Note that the median τ_c and τ_e of the three defect centres are several decades faster for the FE samples. That such defects can both capture and emit electrons in the ns-ms time scale implies they are energetically close to the Fermi level at the silicon surface, and presumably spatially located near the Si surface.

Table IV. Defect parameters for defects centers in HfO₂, Si:HfO₂ and HZO stacks, as deduced from charge capture and emission measurements from temperatures in the range 77- ~400K .

	HfO ₂			Si:HfO ₂			HZO		
	R_1	R_2	R_3	R_1	R_2	R_3	R_1	R_2	R_3
$E_{A_c} \pm \sigma_{E_{A_c}}$ [eV]	1.08±0.33	0.49±0.15	0.25±0.10	1.02±0.30	0.30±0.095	0.15±0.13	0.90±0.29	0.19±0.17	0.15±0.13
$E_{A_e} \pm \sigma_{E_{A_e}}$ [eV]	1.36±0.33	0.46±0.22	0.30±0.11	1.20±0.34	0.27±0.11	0.14±0.13	1.20±0.31	0.22±0.20	0.14±0.13
τ_0 [s]	7.3e-9	2.7e-10	2.4e-14	8.5e-8	6e-8	9.3e-13	8.5e-8	8.5e-9	9.3e-13
$\Delta V_{th_{max}}$ [V]	0.63	0.46	0.59	0.23	0.19	0.57	0.50	0.30	0.57

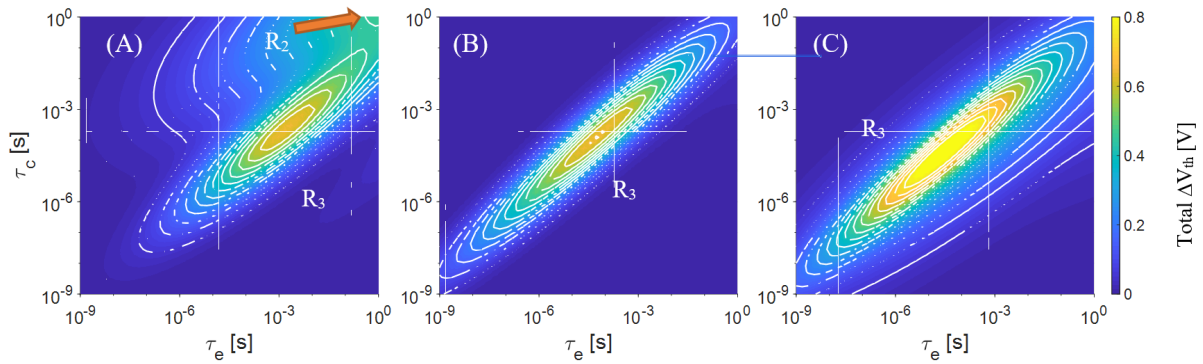


Figure 21. Map of capture and emission times, at 398K, revealing the fast defect centers in (a) HfO₂, (b) Si:HfO₂ and (c) HZO stacks. These defect sub-populations (both R_2 and, predominantly R_3) are centered at lower τ_c and τ_e for ferro stacks and contribute to significant V_{th} shifts on short timescales.

Deliverable D3.4

Impact of stable defect configurations on performances and scaling of HfO_2 -based Fe-devices

Furthermore, capacitors were used to collect polarization-field (PV) and switching-speed (NLS) measurements have identically-processed FE layer in a metal-ferroelectric-metal (MFM) structure, see Figure 22 [cf. Figure 17b].

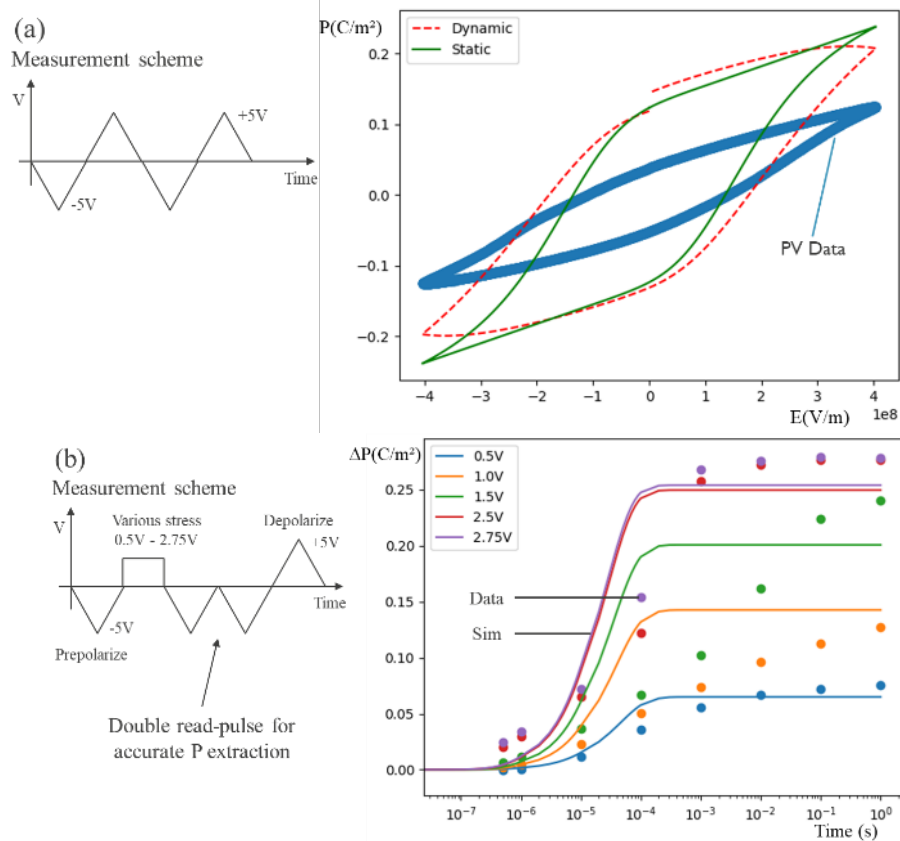


Figure 22. (a) Measured and simulated PV loops on 9.5nm FE capacitors. The left-side figure illustrates the measurement scheme. (b) Switch-speed measurement and simulation using a dynamic FE model. The left-side figure shows the measurement procedure. The model follows the data well at low field, which is the most relevant for the trapping simulation. Parameter values can be found in Table IV.

The MSM data are summarized in Figures 23-25. Results from PV and NLS (Figure 22) are used for the ferroelectric samples. Two defect levels are used, listed in Table V. For times longer than the polarization saturation time we use a static FE model to understand the trapping data (Figure 24), while for shorter times we use a dynamic FE model (Figure 25) [12].

Deliverable D3.4

Impact of stable defect configurations on performances
and scaling of HfO₂-based Fe-devices

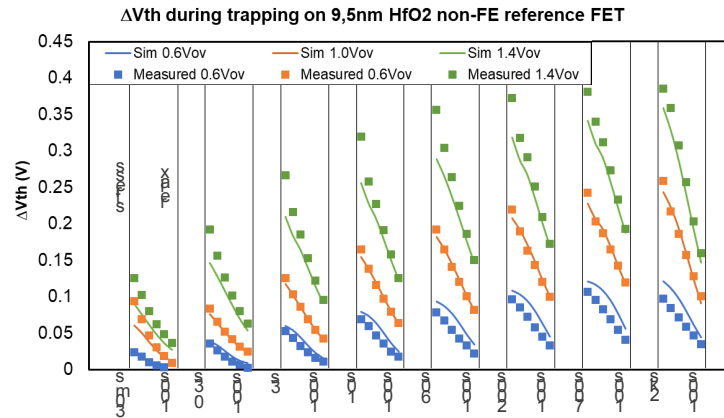


Figure 23. Trapping data (symbols) on non-FE reference device to calibrate the shallow trap bands, measured at 25°C. Only the relax phases are plotted. Time is along the x-axis on a log scale, each phase starts at 50 ms and the duration is shown at the bottom. Lines correspond to simulations with calibrated parameters in Table V.

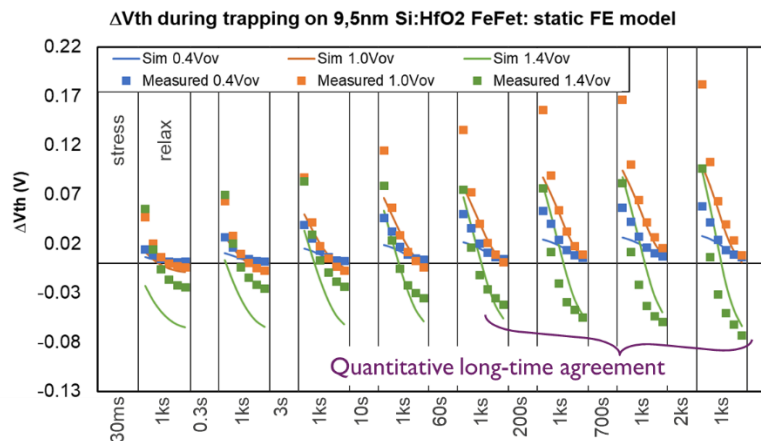


Figure 24. Trapping in FeFET. Box symbols are experimentally extracted ΔV_{th} , lines are simulated with a static FE model (trap parameters in Table II). Only the relax phases are plotted. Time is along the x-axis on a log scale, each phase starts at 50 ms and the duration is shown at the bottom. Quantitative agreement is obtained on the longer timescales.

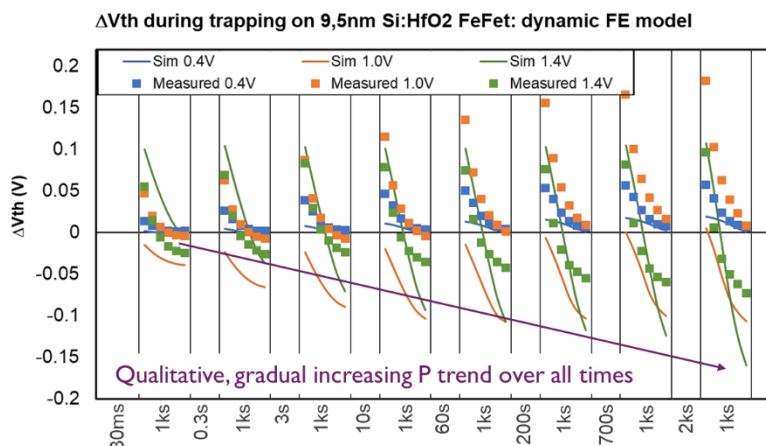


Figure 25. Trapping in FeFET. Boxes are experimentally extracted ΔV_{th} , lines are simulated with a dynamic FE model (FE parameters in Table I, trap parameters in Table II). Only the relax phases are plotted. Time is along the x-axis on a log scale, each phase starts at 50 ms and the duration is shown at the bottom. The simulation shows qualitative agreement over the full-time range, from 30 ms to 2 ks. The dynamic model can describe the gradual polarization change at 1.4 V overdrive. Full quantitative agreement is sensitive to short-time trapping (not included) because of the FE history-dependence. To improve the overall scale of the simulation a 3% P_R prepolarization was used.

Table V. 2-NMP parameter values for the extracted trap bands to reproduce the data in Figure 23. Trap energy levels are w.r.t. Si midgap.

	N_t (m ⁻³)	E_t (eV)	S (eV)	R
IL	2e25	1±0.16	5±2	0.44
High-k	5e25	1±0.19	0.76±0.4	0.59

Conclusion

We presented the activity performed under Task 3.2 about the M2D characterization of FE capacitors and FETs, based on hafnia. The electronic structure parameters of ideal and defective crystalline structure resulting from DFT calculations have been used as material input for the Ginestra[®] device simulation. The results indicate a critical correlation between defect traps (especially oxygen vacancies) and the ferroelectric polarization and thus electrical response and reliability of the final device. This study indicates the huge potentiality of the M2D workflow implemented into the IM2D box, which can be extensively exploited to cover the large range of degree of freedom (doping, temperature, compositions) that affect the experimental data, as confirmed by the recent experimental findings reported at the end of this document.

References

- [1] C. Freysoldt, et al. *Phys. Rev. Lett.* **102**, 016402 (2009); *Phys. Status Solidi B* **248**, 1067 (2011).
- [2] L. Chen, et al. "Ultra-low power Hf 0.5 Zr 0.5 O 2 based ferroelectric tunnel junction synapses for hardware neural network applications," *Nanoscale* **10**, 15826-15833 (2018).
- [3] R. Berdan, et al. "Low-power linear computation using nonlinear ferroelectric tunnel junction memristors." *Nature Electronics* **3**, 259-266 (2020).
- [4] B. Max, et al. "Hafnia-based double-layer ferroelectric tunnel junctions as artificial synapses for neuromorphic computing," *ACS Appl. Elect. Mater.* **2**, 4023-4033 (2020).
- [5] M. Jerry, et al. "Ferroelectric FET analog synapse for acceleration of deep neural network training," 2017 IEEE International Electron Devices Meeting (IEDM).
- [6] H. Mulaosmanovic, et al. "Novel ferroelectric FET based synapse for neuromorphic systems," *Proc. of VLSI Tech. Symposium*.
- [7] M. Jerry, et al. "A ferroelectric field effect transistor based synaptic weight cell," *J. Phys. D: Appl. Phys.* **51**, 434001 (2018).
- [8] H. Mulaosmanovic, et al. "Mimicking biological neurons with a nanoscale ferroelectric transistor," *Nanoscale* **10**, 21755-21763 (2018).
- [9] J. Luo et al. "Capacitor-less stochastic leaky-FeFET neuron of both excitatory and inhibitory connections for SNN with reduced hardware cost," 2019 IEEE International Electron Devices Meeting (IEDM).
- [10] Y. Fang, et al. "Neuro-mimetic dynamics of a ferroelectric FET-based spiking neuron," *IEEE Elec. Dev. Lett.* **40**, 7, 1213-1216 (2019).
- [11] B. J. O'Sullivan, B. Truijen, V. Putcha, A. Grill, A Chasin, G. Van Den Bosch, B. Kaczer, M.N.K. Alam, J. Van Houdt, "Modelling ultra-fast threshold voltage instabilities in Hf-based ferroelectrics", *Proc. Int. Reliability Phys. Symp.(IRPS) 2022*, March 27-31, Dallas, TX, USA.
- [12] B. Truijen, B. O'Sullivan, Md Nur K. Alam, D. Claes, M. Thesberg, P. Roussel, A. Chasin, G. Van den Bosch, B. Kaczer, and J. Van Houdt, "Trap-polarization interaction during low-field trap characterization on hafnia-based ferroelectric gate stacks", *Proc. Int. Reliability Phys. Symp.(IRPS) 2022*, March 27-31, Dallas, TX, USA.

Acronyms

- CBM - Conduction Band Minimum
- CVC - Capacitance-Voltage Characteristics
- DFT - Density Functional Theory
- DoA - Description of the Action
- EOT - Equivalent Oxide Thickness
- FE - Ferroelectric
- FeCap - Ferroelectric Capacitors
- FeFET - Ferroelectric Field Effect Transistors
- FTJ - Ferroelectric Tunnel Junctions

GB - Grain Boundary
GGA - Generalized Gradient Approximation
HVT - High Voltage Threshold
HZO - Zr-doped HfO
IM2D - Interoperable Materials To Device
M2D - Material-To-Device
MAV - Macroscopically Averaged Potential
MFIS - Metal-Ferroelectric-Insulator-Semiconductor
MFM - Metal-Ferroelectric-Metal
NLS - Nucleation Limited Switching
PGL - Poisson-Ginzburg-Landau
PV - Polarization-Field
PV - Polarization-Voltage
VBM - Valence Band Maximum